Journal of Magnetism and Magnetic Materials 594 (2024) 171890

Contents lists available at ScienceDirect

Journal of Magnetism and Magnetic Materials

journal homepage: www.elsevier.com/locate/jmmm

Research article

Site preference of the 3*d* transition metal ions in the $Mn_{4-x}Fe_xNb_2O_9$ compounds as revealed by Mössbauer spectroscopy

Bo Zhang [a,1], Jijun Xue [a,1], Yantao Cao [a,b], Qifeng Kuang [c], Da Li [c], Hanjie Guo [b], ZhenHua Li [d], Liyun Tang [a], Hua Pang [a], Fashen Li [a], Zhiwei Li [a,*]

[a] Key Lab for Magnetism and Magnetic Materials of the Ministry of Education, School of Physical Science and Technology, Lanzhou University, Lanzhou 730000, Gansu, China
[b] Songshan Lake Materials Laboratory, Dongguan 523808, Guangdong, China
[c] Shenyang National Lab for Materials Science, Institute of Metal Research, Chinese Academy of Sciences, and School of Materials Science and Engineering, University of Science and Technology of China, 72 Wenhua Road, Shenyang, 110016, China
[d] Lanzhou Center for Theoretical Physics, Key Laboratory of Quantum Theory and Applications of MOE, Key Laboratory of Theoretical Physics of Gansu Province, Lanzhou University, Lanzhou 730000, Gansu, China

ARTICLE INFO

Keywords:
Site preference
Mossbauer spectroscopy
DFT calculation
Band mixing behavior

ABSTRACT

In this paper, we report on structural, magnetic, Mössbauer spectroscopy and density functional theory (DFT) studies of the $Mn_{4-x}Fe_xNb_2O_9$ compounds. Temperature dependent magnetization measurements have shown that the paramagnetic to antiferromagnetic transition temperatures, T_N, depend non-linearly on the Fe doping level x, which is different from earlier studies on similar compounds of $Mn_{4-x}Co_xNb_2O_9$. More interestingly, our Mössbauer spectroscopy measurements have revealed preferential occupation of the 3*d* transition metal ions, namely, the Fe(Mn) atoms prefer to occupy the highly buckled M-II(relative flat M-I) site, which can be well understood by the band mixing behavior from our DFT calculations. These results are expected to be important for a better understanding of the rich physics of this family of compounds, especially when one concerns the interpretation of experimental results of similar mixing compounds.

1. Introduction

The corundum-type compounds, $M_4A_2O_9$ (M = Mn, Co, Fe, A = Nb, Ta), have been investigated by many groups [1–8] concerning their diverse magnetic structures [5,7–9], linear magnetoelectric (ME) effects [1,2] and magnetism induced spontaneous electric polarizations in the Fe-based compounds [2,3]. The crystal structure of this family of compounds crystallizes in the space group of $P\bar{3}c_1$ at all temperatures with the exception of the $Fe_4Nb_2O_9$ compound, which exhibits a structural transition from $P\bar{3}c_1$ to $C2/c$ upon cooling across ~77 K [8]. This type of crystal structure exhibits two distinct crystallographic sites, the relatively flat M-I site and the highly buckled M-II site, alternating along the *c*-axis. By cooling the samples to lower temperatures, the system changes from paramagnetic (PM) state to antiferromagnetic (AFM) states with ferromagnetic (FM) correlations between adjacent M-I and M-II layers and AFM correlations between nearest neighbor chains along the *c*-axis [5,7–9].

Despite tremendous investigations of this system, the origin of the observed ME effect is still not very clear. It is found that the inverse Dzyaloshinskii–Moriya (DM) interaction [9], namely, the spin-current mechanism, the metal-ligand *p-d* hybridization mechanism [10], and exchange magnetostriction mechanism [11] may play important roles, all of which are highly related to the detailed magnetic structures of the compounds. However, collinear magnetic structures determined by early neutron scattering, AFM orders with spins pointing along the *c*-axis for $Mn_4Nb_2O_9$ and AFM orders with spins lying within the *ab*-plane for $Co_4Nb_2O_9$ and $Fe_4Nb_2O_9$ compounds [12,13], are inconsistent with the observed ME and spontaneous electric polarization effects [2–4]. More recent works have shown that non-collinear magnetic structures may play important roles for a better understanding of the rich physics observed in this system [4,5,7–9].

Clearly, further studies on this system by controlling specific parameters are highly desired. Chemical doping, namely, by mixing the transition metal ions at the M site or mixing the Nb/Ta ions at the A site, has been routinely adopted to gain further information of the studied systems [13–16]. For example, the tuned structural, magnetic [13,14], and ME properties [16] might shed light on the true

* Corresponding author.
E-mail addresses: lizhenhua@lzu.edu.cn (Z. Li), zweili@lzu.edu.cn (Z. Li).
[1] These authors contributed equally to this work.

https://doi.org/10.1016/j.jmmm.2024.171890
Received 22 December 2023; Received in revised form 8 February 2024; Accepted 21 February 2024
Available online 22 February 2024

understanding of this family of compounds. Therefore, in this paper, we made structural and magnetic studies on the $Mn_{4-x}Fe_xNb_2O_9$ series of compounds. Apart from the similar structural changes found for the $Mn_{4-x}Co_xNb_2O_9$ series [13,14], our magnetic measurements revealed non-linear dependence of the PM-AFM transition temperatures, T_N, on the doping level x. More interestingly, our Mössbauer measurements have shown that the Fe atoms prefer to occupy the M-II site, which can be well understood by the help of our density functional theory (DFT) calculations. These results are important regarding the data interpretation of related mixing systems.

2. Experiments

Polycrystalline samples of $Mn_{4-x}Fe_xNb_2O_9$ were prepared by using the conventional solid-state reaction route as described in earlier works [7,17,18]. Stoichiometric amounts of Fe, Fe_2O_3, MnO and Nb_2O_5 powders were thoroughly mixed and then pelletized in a glove box filled with argon. The pellets were reacted at 1100 °C under pure argon atmosphere. This procedure was repeated several times with intermediate grindings to improve the sample quality.

Phase purity was checked by room temperature X-ray powder diffraction (XRPD) and the Rietveld refinements were done by using the FullProf suite [19]. Magnetic properties were measured using a dc superconducting quantum interference device (SQUID) magnetometer (Quantum Design). Room temperature Mössbauer measurements were performed in transmission geometry with a conventional spectrometer working in constant acceleration mode. A 50 mCi γ-ray source of ^{57}Co embedded in Rh matrix vibrating at room temperature was used. The drive velocity was calibrated using sodium nitroprusside (SNP) and the isomer shifts quoted in this paper are relative to that of the α-Fe at room temperature.

For the DFT calculations, we have employed the Vienna *ab initio* simulation package (VASP) code [20,21] for the structural relaxation and the total energy calculations for estimating the spin-exchange parameters. For the exchange correlation functional, generalized gradient approximation (GGA) with the Perdew–Burke–Ernzerhof (PBE) [22] parametrization was used. Projector augmented wave (PAW) [23] potentials were expanded in the plane wave basis with a kinetic energy cutoff of 450 eV. Brillouin zone integration was sampled using a Γ-centered [24] k mesh of $6 \times 6 \times 4$. The total energies were converged to less than 10^{-8} eV to achieve good self consistency in the electronic step and the positions of the ions were relaxed towards the equilibrium position using the conjugate gradient algorithm, until the force acting on each atom is less than 10^{-3} eV/Å. DFT+U method [25] was used to take into account the electron correlation effects for the localized Mn/Fe 3d states in the spherically averaged approach with U_{eff} = 3.1 eV.

For the density of states (DOS) calculations, we have used the full potential linearized augmented plane wave (FP-LAPW) method as implemented in the ELK code [26]. The Perdew–Wang/Ceperley–Alder local spin density approximation (LSDA) exchange–correlation functional [27] was used. LSDA+U calculations were done in the fully localized limit (FLL) and by means of the Yukawa potential method [28] with a screening length of λ = 3.0 for both Mn and Fe 3d electrons. The resulting U/J parameters are U = 2.32 eV and J = 0.74 eV for the Mn atoms and U = 2.63 eV and J = 0.80 eV for the Fe atoms, respectively. The plane-wave cutoff was set to $R_{MT} \times |\mathbf{G}+k|_{max}$ = 7.0 Hartree. and the maximum $\mathbf{G}$ vector for the potential and density was set to $|\mathbf{G}|_{max}$ = 12.0 Hartree. The Γ-centered k-point mesh of $6 \times 6 \times 4$ was used. We have also checked other parameters and found that the electron correlation effects U have to be included in addition to the AFM order for the $Fe_4Nb_2O_9$ compound to open the energy gap at the Fermi level in accordance with the experimentally observed insulating nature of the material. Whereas for the $Mn_4Nb_2O_9$ compound, the AFM order is already enough for the opening of the gap. Other U parameters will result in different gap sizes but have no effects concerning the main conclusions of this paper, and thus were not reported here.

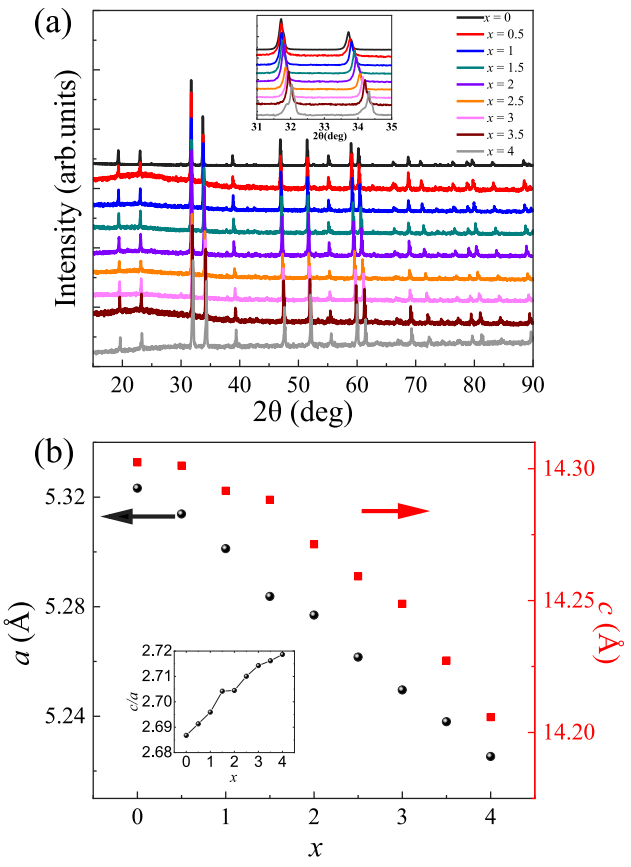

Fig. 1. (a) Room temperature X-ray powder diffraction (XRPD) data of $Mn_{4-x}Fe_xNb_2O_9$ compounds. (b) Lattice parameters a and c of $Mn_{4-x}Fe_xNb_2O_9$, extracted by Rietveld refinements of the XRPD data shown in (a), as a function of doping level x. Inset of (a) shows an enlarged view of the main peaks in the range of 31° ~ 35° for a better view of the peak shifts upon doping. Inset of (b) shows the ratio of c/a upon increasing x.

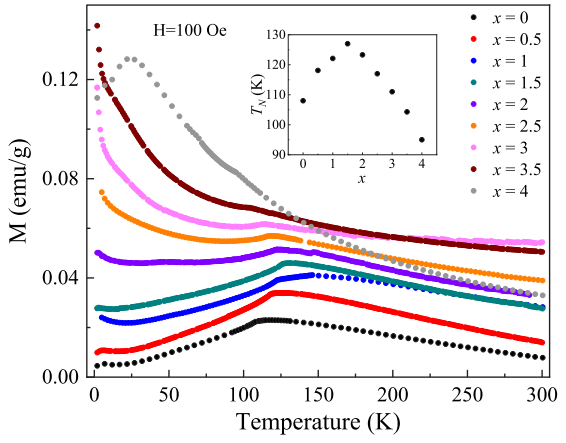

Fig. 2. Temperature dependence of the magnetization, $M(T)$, of the $Mn_{4-x}Fe_xNb_2O_9$ family measured with an external field of 0.01 T. Inset shows the extracted T_N vs x of the $Mn_{4-x}Fe_xNb_2O_9$ series. The red arrows are guides for the eye.

3. Results and discussion

In Fig. 1(a), we show the room temperature XRPD patterns of the $Mn_{4-x}Fe_xNb_2O_9$ compounds. Consistent with earlier reports, these data indicate that our samples exhibit the desired 429-phase (space group

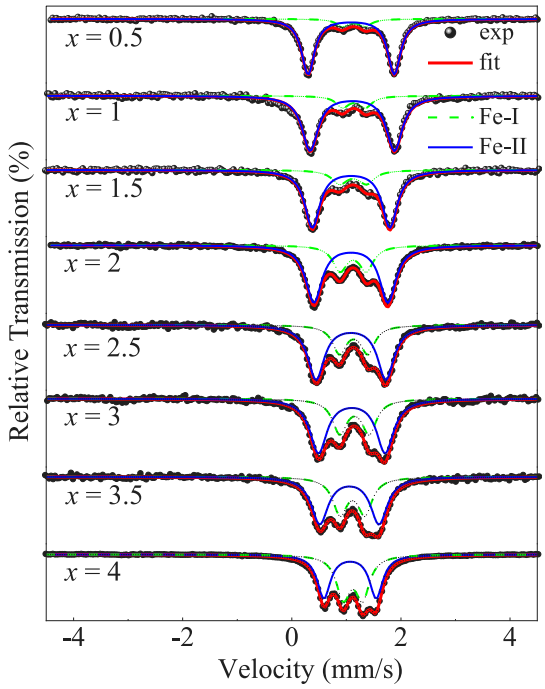

Fig. 3. ^{57}Fe Mössbauer spectra (black dots) of $Mn_{4-x}Fe_xNb_2O_9$ samples measured at room temperature. Solid lines are fits to the experimental data with two doublets as described in the text.

P$\bar{3}$c1) with a small amount of the 126-phase impurities $FeNb_2O_6$/$MnNb_2O_6$, which is usual for powder samples of this system [7,17,18]. To determine the fraction of the impurity 126-phase and the doping dependence of the lattice parameters, we made Rietveld refinements of the data shown in Fig. 1(a) by using the FullProf suite [19] (see Fig. S1 in the supplemental materials for the refined patterns). The refined percentage of the 126-phase is rather small, which is similar to our earlier work on the $Co_4Nb_2O_9$ sample [7]. The determined lattice parameters as a function of doping level x are shown in Fig. 1(b), with a = 5.3233(1) Å, c = 14.3024(2) Åfor $Mn_4Nb_2O_9$ and a = 5.2251(1) Å, c = 14.2057(2) Åfor $Fe_4Nb_2O_9$, which is in agreement with previous reports [18,29]. One can see that both a and c decrease monotonically with increasing x due to the smaller Fe^{2+} ion size than the Mn^{2+} ion, which is similar to the Co-doped case of both $Mn_{4-x}Co_xNb_2O_9$ single crystals [14] and powder samples [13]. As shown in the inset of Fig. 1(b), the c/a ratio has a small increase with increasing x, suggesting a stretching along the c-axis direction with increasing x.

Fig. 2 displays the magnetization, $M(T)$, as a function of temperature of the $Mn_{4-x}Fe_xNb_2O_9$ family measured under an external magnetic field of 0.01 T. The temperature dependent behavior changes gradually from that of the pure $Mn_4Nb_2O_9$ compound to that of the pure $Fe_4Nb_2O_9$ compound as expected. The PM-AFM transition temperatures, T_N, determined from the kink of the $M(T)$ curve are shown in the inset of Fig. 2 as a function of doping level x. Interestingly, with increasing doping x, T_N first increases to a maximum value of $T_N(x = 1.5) = 127$ K and then decreases again. This is different with the linear dependent behavior of the Co-doped case [14] (see Fig. S2 in the supplemental materials for a comparison), suggesting a more complex dependence of the exchange energy on the doping of Fe for the Mn atoms than the Co-doped series, which deserves further investigations with neutron scattering to fully determine the exchange parameters, J_{ij}, as a function of doping x.

To probe the local properties of the doped Fe atoms, we performed ^{57}Fe Mössbauer measurements at room temperature. As shown in Fig. 3, the measured Mössbauer spectra were fitted with two doublets corresponding to the two inequivalent crystallographic sites, namely, the relative flat Mn/FeO_6 layer (site M-I) and the highly buckled Mn/FeO_6 layer (site M-II), which is similar to our previous studies on the $Co_{0.97}Fe_{0.03}Nb_2O_9$ samples [7]. The good matching of the fitted theoretical curves (red lines in Fig. 3) with the experimental data points and the absence of any other absorption peaks indicate that the 126-impurity phase shown up in our XRPD measurements is below the detection limit of our Mössbauer spectrometer, which again proves the good quality of our samples.

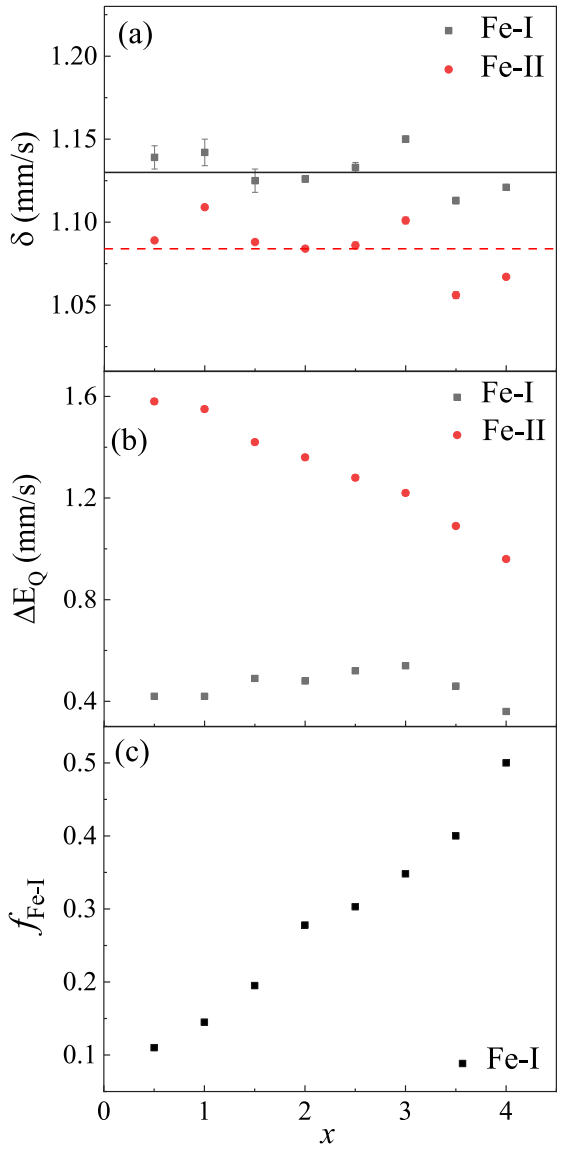

Fig. 4. Doping dependence of the determined hyperfine parameters (a) isomer shift, δ (mm/s), (b) quadrupole splitting, ΔE_Q (mm/s), and (c) the fraction of the Fe atoms at site M-I. Lines in (a) are only guides for the eye.

The determined hyperfine parameters, namely, the isomer shifts (δ) and quadrupole splitting ($\Delta E_Q = eQV_{zz}/2$), are shown in Fig. 4(a) and (b), respectively. With increasing x, the δ values of both the Fe-I and the Fe-II sites do not change very much and the values are in the range of 1.05 mm/s~1.15 mm/s, which is typical for the high-spin Fe^{2+} (d^6, S = 2) located in the FeO_6 octahedrons [7,31]. These data are consistent with our X-ray photoelectron spectroscopy (XPS) measurements as shown in Fig. S3 in the supplemental materials. The ΔE_Q for the Fe-I site shows only a minor increase with increasing x to about x = 3.0 and then decrease again. On the other hand, the ΔE_Q for the Fe-II site exhibits a clear decrease with increasing x. The

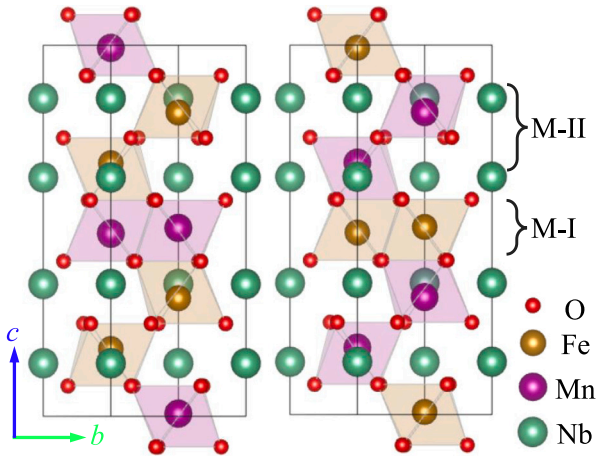

Fig. 5. Side view of the two model structures ($x = 2$) constructed for $Mn_2Fe_2(I)Nb_2O_9$ (right) and $Mn_2Fe_2(II)Nb_2O_9$ (left) compounds in our DFT calculations. The alternate stacking of the Fe-layers and Mn-layers along the c-axis can be seen. The crystal structures were drawn by using the software VESTA [30].

Table 1
Relaxed structural parameters for $Mn_4Nb_2O_9$, $Fe_4Nb_2O_9$ and the two model strictures $Mn_2Fe_2(I)Nb_2O_9$ and $Mn_2Fe_2(II)Nb_2O_9$ as shown in Fig. 5. Lattice constants have been kept fixed at the experimental values. The trigonal structure with space group $P\bar{3}c1$ was used for all the compounds despite that the $Fe_4Nb_2O_9$ compound exhibits a structural transition at ~77 K to the monoclinic structure with space group $C2/c$ [8].

$Mn_4Nb_2O_9$	:	$a = b = 5.3233$ Å,	$c = 14.30239$ Å
Atom	x/a	y/b	z/c
Mn-I	1/3	2/3	0.018067
Mn-II	1/3	2/3	0.302930
Nb	0	0	0.357681
O1	0.278883	0	1/4
O2	0.336581	0.309946	0.085670
$Fe_4Nb_2O_9$	:	$a = b = 5.2253$ Å,	$c = 14.20580$ Å
Atom	x/a	y/b	z/c
Fe-I	1/3	2/3	0.013713
Fe-II	1/3	2/3	0.306774
Nb	0	0	0.358167
O1	0.285742	0	1/4
O2	0.337282	0.317679	0.084011
$Mn_2Fe_2(I)Nb_2O_9$	:	$a = b = 5.2769$ Å,	$c = 14.27131$ Å
Atom	x/a	y/b	z/c
Fe-I	1/3	2/3	0.013524
Mn-II	1/3	2/3	0.305552
Nb	0	0	0.358365
O1	0.280005	0	1/4
O2	0.334518	0.315577	0.083252
$Mn_2Fe_2(II)Nb_2O_9$	:	$a = b = 5.2769$ Å,	$c = 14.27131$ Å
Atom	x/a	y/b	z/c
Mn-I	1/3	2/3	0.015999
Fe-II	1/3	2/3	0.306821
Nb	0	0	0.356959
O1	0.285275	0	1/4
O2	0.337517	0.312645	0.086330

decrease of ΔE_Q suggests either a gradual structural change and/or a purely electronic origin, such as a different orbital occupation with increasing x. From the crystal structure, the local symmetry of the Mn/Fe atoms are $D3d$ for both sites, which means that the main crystal field effect on the $3d$ orbitals is the $t_{2g} - e_g$ splitting in the octahedral MO_6 environments. But, the t_{2g} levels are further split into lower-energy doublet $e_g^{\pi}(d_{xy}, d_{x^2-y^2})$ and higher-energy singlet $a_{1g}(d_{z^2})$ [32]. As observed from the XRPD measurements, the small increase of the c/a ratio will change the relative energy levels of these orbitals. This may lead to a redistribution of the $3d$ electrons among these orbitals as also suggested by our DFT calculations. Then, the redistribution of the $3d$ electrons shall be responsible for the observed decrease of ΔE_Q with increasing x [31].

More interestingly, we observe a different occupation fraction of the Fe atoms for the two crystallographic sites (as labeled with M-I and M-II) especially for smaller x values. In a Mössbauer experiment, the ratio of the Fe atoms siting at two different sites can be estimated by the intensity ratio of the corresponding subspectrum (here the two doublets) if the similar recoilless factor were assumed for both sites. The relative fraction for site Fe-I ($f_{\text{Fe-I}}$) as a function of x is shown in Fig. 4(c). Clearly, $f_{\text{Fe-I}}$ increases almost linearly from 0 at $x = 0$ to 0.5 at $x = 4$, consequently, $f_{\text{Fe-II}} = 1 - f_{\text{Fe-I}}$ decreases linearly from 1.0 at $x = 0$ to 0.5 at $x = 4$. This indicates that the Fe atoms are more readily to occupy the M-II site at lower x values. Site preferential occupation is not rare, but usually found in samples with distinctly different sites with large volume differences, such as tetrahedrons vs octahedrons etc. [33–37]. In certain cases, the volume difference can be as large as ~ 17% between two different sites [34]. While, in our case here, the volume difference is rather small for the two different sites, e.g. ~ 1.4% for $Fe_4Nb_2O_9$ [8] and the differences for our DFT relaxed structures (as shown in Table 1) are all smaller than ~ 5%. This suggests that there must be other forces instead of the simple volume-difference picture that drives the Fe atoms into the M-II site.

To better understand the above observed experimental results, we made first-principle DFT calculations. The crystal structures of $Mn_4Nb_2O_9$, $Fe_4Nb_2O_9$ and the two model structures for $x = 2$, namely, $Mn_2Fe_2(I)Nb_2O_9$ with the Fe atoms occupy only the M-I site and $Mn_2Fe_2(II)Nb_2O_9$ with the Fe atoms occupy only the M-II site as shown in Fig. 5, were relaxed by using the VASP code while keeping the lattice constants fixed at the experimentally determined values. The relaxed structural parameters are shown in Table 1. The relaxed atomic positions show reasonable agreement with previously published data for the two ending members [8,12].

First, we consider the non-linear doping dependence of the AFM transition temperature T_N as observed in our magnetization measurements (see the inset of Fig. 2). In systems with local magnetic spins S_i and S_j interacting through the nearest-neighbor (NN) exchange constant J_{ij} can be modeled with the Heisenberg Hamiltonian

$$H = \frac{1}{2} J_{ij} \sum_{ij} S_i \cdot S_j. \tag{1}$$

Then the AFM transition temperature for a system with non-identical spin-exchange parameters may be estimated by the following equation [38]

$$T_N \sim \frac{S(S+1) \sum_j^z J_{ij}}{3k_B}, \tag{2}$$

where z is the total number of spins that have interactions with spin S_i. Therefore, T_N should be approximately proportional to the average spin-exchange parameter for a system with different kinds of spins interactions. As shown in Fig. 6, several NN interactions have been considered by Deng et al. for $Mn_4Nb_2O_9$ [11] and $Co_4Nb_2O_9$ [9]. For $Co_4Nb_2O_9$, all the five NN interactions are small with absolute values smaller than ~ 1 meV, which is consistent with the observed low T_N ~ 27 K [4]. For $Mn_4Nb_2O_9$, the determined values are $J_1 = 3.38$ meV and $J_2 = 1.307$ meV, and the transition temperature was found to be as high as ~ 109 K [17]. Other interactions are at least one order of magnitude smaller [11]. Therefore, to simplify our calculation, we consider to estimate only J_1 and J_2 by using three AFM orders as shown in Fig. 6, AFM1-3, where other interactions (J_3-J_4-J_5) will cancel out in the Hamiltonian for these magnetic structures. The simple FM structure and the AFM4 magnetic order, which was reported experimentally [7,8,12,13] to be the ground state magnetic structure, were also calculated for a complete comparison.

The calculated total energies and magnetic moments at the M-I and M-II sites of the four relaxed crystal structures with different magnetic

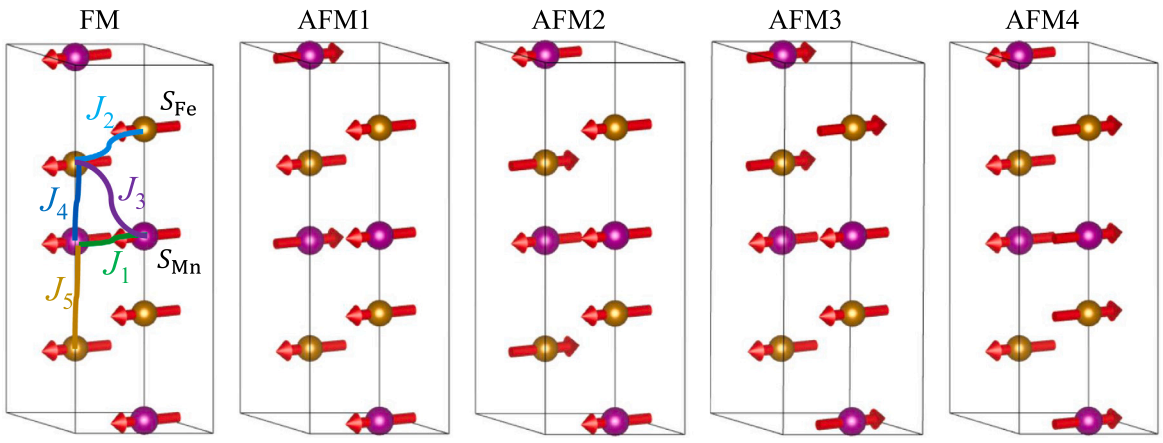

Fig. 6. Various magnetic structures considered in our DFT calculations to estimate the nearest-neighbor (NN) spin-exchange interaction parameters J_{ij} between different spins S_i and S_j. The crystal structures were drawn by using the software VESTA [30].

Table 2
Calculated total energies E (eV/u.c.) and magnetic moments μ (μ_B) of different magnetic structures shown in Fig. 6 for the relaxed crystal structures listed in Table 1. The estimated spin-exchange parameters J_1 and J_2 (meV) are also listed in the last two rows.

	$Mn_4Nb_2O_9$			$Fe_4Nb_2O_9$			$Mn_2Fe_2(I)Nb_2O_9$			$Mn_2Fe_2(II)Nb_2O_9$		
	E	$\mu_{Mn\text{-}I}$	$\mu_{Mn\text{-}II}$	E	$\mu_{Fe\text{-}I}$	$\mu_{Fe\text{-}II}$	E	$\mu_{Fe\text{-}I}$	$\mu_{Mn\text{-}II}$	E	$\mu_{Mn\text{-}I}$	$\mu_{Fe\text{-}II}$
FM	−255.60197	4.582	4.581	−237.23598	3.701	3.805	−247.47530	3.722	4.574	−247.72670	4.571	3.727
AFM1	−255.84746	4.556	4.547	−237.50317	3.678	3.665	−247.52305	3.690	4.537	−246.83022	4.547	3.681
AFM2	−255.86233	4.562	4.575	−239.65632	3.681	3.732	−247.70204	3.711	4.563	−247.89565	4.554	3.700
AFM3	−255.70561	4.574	4.550	−237.93319	3.699	3.673	−247.53717	3.702	4.548	−246.68181	4.559	3.699
AFM4	−256.02888	4.574	4.574	−239.68112	3.694	3.735	−247.76800	3.703	4.571	−248.12068	4.569	3.712
J_1		0.565			−2.626			−0.086			0.593	
J_2		0.624			10.293			0.658			7.341	

models are listed in Table 2. Clearly, for all these compounds, the AFM4 magnetic model exhibits the lowest energy. This is consistent with the experimentally reported magnetic structures [7,8,12,13]. The calculated magnetic moments for the Mn and the Fe atoms, which are very close to each other for both the M-I and the M-II sites, are a little smaller than the theoretical value of $\mu_{Mn} = gS = 5.0\ \mu_B$ and $\mu_{Fe} = 4.0\ \mu_B$ (g is the Landé factor). However, the moments determined from the Curie–Weiss fitting of the $\chi(T)$ data are considerably larger than the theoretical value [4,7,18,29]. These results suggest that there must be a contribution to the total magnetic moments from the orbital part, which we have neglected in our current calculations.

The magnetic energies of the AFM1-3 magnetic structures shown Fig. 6 can be expressed using the NN Heisenberg Hamiltonian (Eq. (1))

$$E_{AFM1} - E_0 = -6J_1S_I^2 + 6J_2S_{II}^2 \quad (3)$$

$$E_{AFM2} - E_0 = 6J_1S_I^2 - 6J_2S_{II}^2 \quad (4)$$

$$E_{AFM3} - E_0 = 6J_1S_I^2 + 6J_2S_{II}^2 \quad (5)$$

where $E_{AFM1\text{-}3}$ denotes the magnetic energy of the corresponding magnetic structure as listed in Table 2 and E_0 is an accessorial parameter that describes the total energy without involving the part of the spin-exchange interaction energy. The derived spin-exchange parameters J_1 and J_2 are listed in the last two rows of Table 2. Our estimated values of J_1 and J_2 for $Mn_4Nb_2O_9$ are both AFM, which is consistent with that obtained by Deng et al. [11] using inelastic neutron scattering, but the values are considerably smaller. This may be caused by the too simplified model we have employed. However, we believe that the relative trend should hold when compared between different compounds calculated with the same method in this paper. For $Fe_4Nb_2O_9$, the estimated absolute values are much larger with J_1 being FM and J_2 being AFM. The different nature between J_1 and J_2 should introduce additional frustration in addition to the honeycomb lattice geometry for the ground state magnetic structure, which explains well the fact that the T_N of $Fe_4Nb_2O_9$ is a little lower than that of $Mn_4Nb_2O_9$. The FM J_1 interaction is also found for $Co_4Nb_2O_9$ by Deng et al. [9] using inelastic neutron scattering, but with much smaller absolute values. Importantly, as shown in Table 2, when the Fe atoms occupy the M-II site the resulting J_2 increases considerably when compared with the J_2 of $Mn_4Nb_2O_9$. On the other hand, when the Fe atoms occupy the M-I site the resulting J_1 is much smaller than that of $Mn_4Nb_2O_9$. The total energy difference between the two model structures for $x = 2$ with the AFM4 ground state amounts to $\Delta E = E[Mn_2Fe_2(I)Nb_2O_9] - E[Mn_2Fe_2(II)Nb_2O_9] = 353$ meV/u.c., which means that the $Mn_2Fe_2(II)Nb_2O_9$ structure has a lower energy, as being consistent with our Mössbauer results, that is the M-II site is energetically preferred to be occupied by the Fe atoms. This explains naturally the observed non-linear doping dependence of the AFM transition temperature T_N since the Fe atoms first enter into the M-II site, leading to an increase of J_2, and then enter into the M-I site, leading to a decrease of the J_1, with increasing x.

As mentioned above, the site volume difference is not large enough to account for the observed site preference of the Mn/Fe ions in $Mn_{4-x}Fe_xNb_2O_9$. Therefore, to unravel the microscopic origin of the site preference, we compare the total and partial density of state (PDOS) of the two model compounds ($x = 2$) with the two ending members of $Mn_4Nb_2O_9$ and $Fe_4Nb_2O_9$ in Fig. 7. Clearly, the 3d electrons from the Mn/Fe atoms are distributed into almost separate energy bands with minor overlap between the M-I and M-II sites. Interestingly, the electron bands of the two model compounds ($x = 2$) can be viewed as a simple mixing of the electron bands from the corresponding M-I and M-II sites of the two ending members but with some shifts towards higher or lower energies. For $Mn_2Fe_2(I)Nb_2O_9$, the band mixing results in a shift of the electron bands towards higher energy for the Fe-I site and a shift for the Mn-II site towards lower energy when compared to the two ending members. On the other hand, for the $Mn_2Fe_2(II)Nb_2O_9$ compound, the band mixing leads to shifts of the electron bands towards lower energies for both the Mn-I and the Fe-II sites, which shall give a much larger energy gain than the $Mn_2Fe_2(I)Nb_2O_9$ compound.

We now discuss the energy reduction for the observed preferential occupation of the M-II site by the Fe atoms that stems from the spin

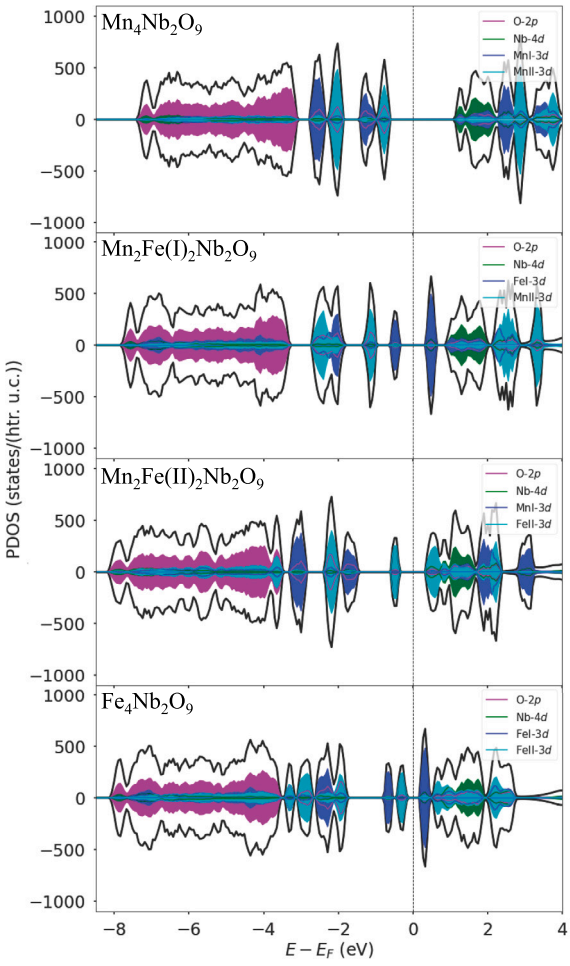

Fig. 7. Comparison of the total and partial densities of states (PDOS) between the $Mn_4Nb_2O_9$, $Mn_2Fe_2(I)Nb_2O_9$, $Mn_2Fe_2(II)Nb_2O_9$, and $Fe_4Nb_2O_9$ compounds.

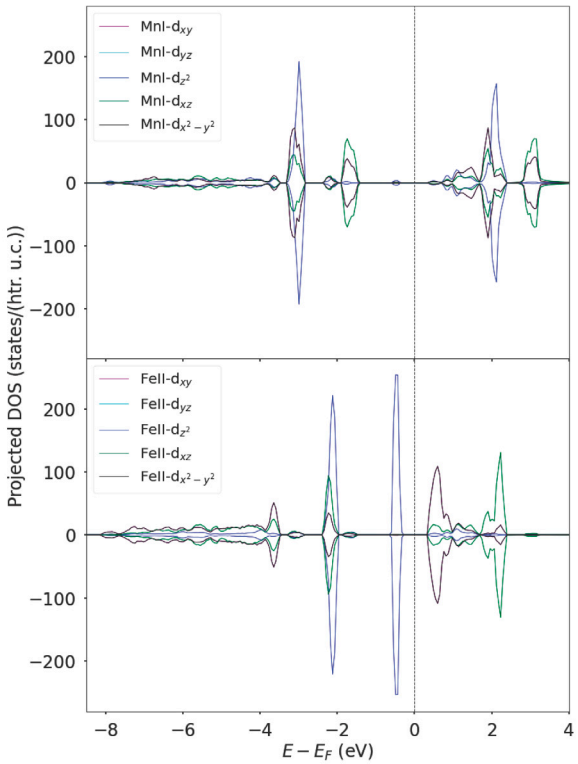

Fig. 8. Projected density of states (DOS) of the $Mn_2Fe_2(II)Nb_2O_9$ compound at the two sites, namely, the Mn-I site (upper panel) and the Fe-II site (lower panel).

exchange interaction. From the structure point of view, the alternating sites, i.e. M-I sites and M-II sites, construct a Heisenberg chain. The exchange interaction inside the chain is determined by the parameters J_4 and J_5, see Fig. 6, whose contributions to the magnetic Hamiltonian are cancelled out by choosing our subtly tailored three AFM structures i.e. AFM1-3. This is also true for the inter-chain exchange interaction J_3. As reported for the $Mn_4Nb_2O_9$ compound, J_3, J_4, and J_5 are rather small compared to J_1 and J_2 [11]. Therefore, we highlight the inter-chain exchange interactions J_1 and J_2 between the M-I sites and the M-II sites, respectively. From our DFT results, see Table 2, when the Fe atoms occupy the M-II sites, it leads to a larger inter-chain AFM exchange interaction of 7.341 meV, by contrast, it leads to a FM exchange interaction of −0.086 meV when the Fe atoms occupy the M-I sites. Meanwhile, the Mn-Mn AFM exchange interactions are nearly unchanged, which is 0.593 meV for the Mn atoms occupying the M-I sites and 0.658 meV for the Mn atoms occupying the M-II sites. The strong AFM exchange interaction between the Fe atoms at the M-II site contribute much to the reduction of the total energy, and thus favoring the $Mn_2Fe_2(II)Nb_2O_9$ structure.

Moreover, for the $Fe_4Nb_2O_9$ compound, we also observe two additional bands from the Fe-II site between the bands of the Fe-I site and the O-2p bands. These bands are merged with the O-2p bands in the $Mn_2Fe_2(II)Nb_2O_9$ compound due to the shift of these bands to lower energies, which shall enhance, to some extend, the hybridization effect between the Fe-II-3d electrons and the O-2p electrons since hybridization between the M-3d states and the O-2p states is typical for the MO_6 octahedron local environment. This enhanced hybridization or covalency effect shall give a more stable connectivity between the Fe-II atoms and the O atoms and thus results in a further lowering of the energy levels for the $Mn_2Fe_2(II)Nb_2O_9$ compound as observed for the $FeMgSiO_4$ olivine compound [34].

To see the orbital character of the 3d electrons, we present the projected density of states at both the Mn-I and the Fe-II sites of the $Mn_2Fe_2(II)Nb_2O_9$ compound in Fig. 8. Clearly, the involved orbitals at the Fe-II site are mainly d_{z^2} with some contributions from the d_{xz}/d_{yz} and $d_{xy}/d_{x^2-y^2}$ orbitals. Then, the energy shifts after the band mixing as discussed above may result in a redistribution of the 3d electrons among these orbitals. This is consistent with the observed decrease of the quadrupole splitting ΔE_Q with increasing x at the Fe-II site. While for the Fe-I site, the observed energy shift is less significant and thus the almost constant value of the observed ΔE_Q in our Mössbauer measurements can be understood.

4. Summary

In summary, we have made structural, magnetic, Mössbauer spectroscopy and DFT studies on the $Mn_{4-x}Fe_xNb_2O_9$ compounds. Our XRPD results have shown that the lattice parameters change gradually with doping level x between the two ending members. On the other hand, our magnetization measurements have revealed non-linear dependence of the PM-AFM transition temperatures, T_N, on the Fe context x, which is different from earlier studies on the $Mn_{4-x}Co_xNb_2O_9$ samples, suggesting a more complex dependent behavior of the magnetic exchange parameters, J_{ij}, on doping level x. Moreover, our Mössbauer spectroscopy results have revealed the preferential occupation of the transition metal ions, namely, the Fe(Mn) atoms prefer to occupy the M-II(M-I) site. These results can be well understood with our DFT calculations, which show that the band mixing behavior, the resulting different spin-exchange parameters, and the hybridization effect may

play important roles. We anticipate that these results may shed important light on interpretation of the experimental data of similar mixing compounds.

CRediT authorship contribution statement

Bo Zhang: Writing – original draft, Investigation. **Jijun Xue:** Methodology. **Yantao Cao:** Investigation. **Qifeng Kuang:** Investigation. **Da Li:** Writing – review & editing, Funding acquisition. **Hanjie Guo:** Writing – review & editing. **ZhenHua Li:** Writing – review & editing, Supervision, Funding acquisition. **Liyun Tang:** Methodology. **Hua Pang:** Writing – review & editing. **Fashen Li:** Supervision. **Zhiwei Li:** Writing – review & editing, Project administration, Funding acquisition.

Declaration of competing interest

The authors declare that they have no known competing financial interests or personal relationships that could have appeared to influence the work reported in this paper.

Data availability

Data will be made available on request.

Acknowledgments

This paper was supported by the National Natural Science Foundation of China (Grants No. 52371203 and No. 12247101) and the National Key Research and Development Program of China (Grant No. 2022YFB4101401). The authors are grateful to the support provided by the Supercomputing Center of Lanzhou University.

Appendix A. Supplementary data

Supplementary material related to this article can be found online at https://doi.org/10.1016/j.jmmm.2024.171890.

References

[1] S.N. Panja, P. Manuel, S. Nair, Phys. Rev. B 103 (2021) 014422.
[2] S.N. Panja, L. Harnagea, J. Kumar, P.K. Mukharjee, R. Nath, A.K. Nigam, S. Nair, Phys. Rev. B 98 (2018) 024410.
[3] A. Maignan, C. Martin, Phys. Rev. Mater. 2 (2018) 091401(R).
[4] N.D. Khanh, N. Abe, H. Sagayama, A. Nakao, T. Hanashima, R. Kiyanagi, Y. Tokunaga, T. Arima, Phys. Rev. B 93 (2016) 075117.
[5] L. Ding, M. Lee, T. Hong, Z. Dun, R. Sinclair, S. Chi, H.K. Agrawal, E.S. Choi, B.C. Chakoumakos, H. Zhou, H. Cao, Phys. Rev. B 102 (2020) 174443.
[6] J. Zhang, N. Su, X. Mi, M. Pi, H. Zhou, J. Cheng, Y. Chai, Phys. Rev. B 103 (2021) L140401.
[7] B. Zhang, Q. Kuang, H. Pang, F. Li, L. Tang, D. Li, Z. Li, J. Magn. Magn. Mater. 575 (2023) 170738.
[8] R. Jana, D. Sheptyakov, X. Ma, J.A. Alonso, M. Pi, A. Muñoz, Z. Liu, L. Zhao, N. Su, S. Jin, X. Ma, K. Sun, D. Chen, S. Dong, Y. Chai, S. Li, J. Cheng, Phys. Rev. B 100 (2019) 094109.
[9] G. Deng, Y. Cao, W. Ren, S. Cao, A.J. Studer, N. Gauthier, M. Kenzelmann, G. Davidson, K.C. Rule, J.S. Gardner, P. Imperia, C. Ulrich, G.J. McIntyre, Phys. Rev. B 97 (2018) 085154.
[10] J.H. Zhang, Y.S. Tang, L. Lin, L.Y. Li, G.Z. Zhou, B. Yang, L. Huang, X.Y. Li, G.Y. Li, S.H. Zheng, M.F. Liu, M. Zeng, D. Wu, Z.B. Yan, X.K. Huang, C. Chen, X.P. Jiang, J.-M. Liu, Phys. Rev. B 107 (2023) 024108.
[11] G. Deng, G. Zhao, S. Zhu, Z. Feng, W. Ren, S. Cao, A. Studer, G.J. McIntyre, New J. Phys. 24 (2022) 083007.
[12] E. Bertaut, L. Corliss, F. Forrat, R. Aleonard, R. Pauthenet, J. Physics and Chemistry of Solids 21 (1961) 234.
[13] B. Schwarz, D. Kraft, R. Theissmann, H. Ehrenberg, J. Magn. Magn. Mater. 322 (2010) L1.
[14] Y. Yu, G. Deng, Y. Cao, G.J. McIntyre, R. Li, N. Yuan, Z. Feng, J.-Y. Ge, J. Zhang, S. Cao, Ceram. Int. 45 (2019) 1093.
[15] A. Maignan, C. Martin, E. Tailleur, F. Damay, M. Mostovoy, X. Wang, Z. Hu, H.-J. Lin, C.-T. Chen, L.H. Tjeng, E. Suard, F. Fauth, 9, (2021) 14236.
[16] S. Zheng, M. Liu, G. Zhou, X. Li, L. Lin, Z. Yan, J.-M. Liu, Ceram. Int. 47 (2021) 14041.
[17] Y. Fang, W.P. Zhou, S.M. Yan, R. Bai, Z.H. Qian, Q.Y. Xu, D.H. Wang, Y.W. Du, J. Appl. Phys. 117 (2015) 17B712, https://pubs.aip.org/aip/jap/article-pdf/doi/10.1063/1.4913815/15160972/17b712_1_online.pdf.
[18] A. Maignan, C. Martin, Phys. Rev. B 9 (2018) 161106.
[19] The FullProf Suite, http://www.ill.eu/sites/fullprof/.
[20] G. Kresse, J. Furthmüller, Phys. Rev. B 54 (1996) 11169.
[21] G. Kresse, J. Furthmüller, Comput. Mater. Sci. 6 (1996) 15.
[22] J.P. Perdew, K. Burke, M. Ernzerhof, Phys. Rev. Lett. 77 (1996) 3865.
[23] P.E. Blöchl, Phys. Rev. B 50 (1994) 17953.
[24] H.J. Monkhorst, J.D. Pack, Phys. Rev. B 13 (1976) 5188.
[25] S.L. Dudarev, G.A. Botton, S.Y. Savrasov, C.J. Humphreys, A.P. Sutton, Phys. Rev. B 57 (1998) 1505.
[26] The Elk Code, http://elk.sourceforge.net/.
[27] J.P. Perdew, Y. Wang, Phys. Rev. B 45 (1992) 13244.
[28] A.I. Liechtenstein, V.I. Anisimov, J. Zaanen, Phys. Rev. B 52 (1995) R5467.
[29] S.H. Zheng, G.Z. Zhou, X. Li, M.F. Liu, Y.S. Tang, Y.L. Xie, M. Zeng, L. Lin, Z.B. Yan, X.K. Huang, X.P. Jiang, J.-M. Liu, Appl. Phys. Lett. 117 (2020) 072903, https://pubs.aip.org/aip/apl/article-pdf/doi/10.1063/5.0021623/14537784/072903_1_online.pdf.
[30] K. Momma, F. Izumi, J. Appl. Crystallogr. 44 (2011) 1272.
[31] P. Gütlich, E. Bill, A.X. Trautwein, MÖssbauer Spectroscopy and Transition Metal Chemistry, Springer Berlin Heidelberg.
[32] I.V. Solovyev, T.V. Kolodiazhnyi, Phys. Rev. B 94 (2016) 094427.
[33] Y. Ji, Y. Ding, W. Wang, H. Wang, J. Yang, X. Shen, Y. Yao, R. Yu, Solid State Commun. 344 (2022) 114666.
[34] S. Chatterjee, S. Sengupta, T. Saha-Dasgupta, K. Chatterjee, N. Mandal, Phys. Rev. B 79 (2009) 115103.
[35] C.R. Quan, J.G. Zhao, Y.Z. Wang, L. Yin, B.G. Shen, Z.X. Cheng, Y.F. Cheng, S.W. Niu, Phys. Rev. B 42 (1990) 6697.
[36] M. Eibschütz, M.E. Lines, H.S. Chen, J.V. Waszczak, G. Papaefthymiou, R.B. Frankel, Phys. Rev. Lett. 59 (1987) 2443.
[37] J.T. Lim, C.S. Kim, J. Appl. Phys. 115 (2014) 17D706, https://pubs.aip.org/aip/jap/article-pdf/doi/10.1063/1.4861676/14117875/17d706_1_online.pdf.
[38] D.C. Johnston, R.J. McQueeney, B. Lake, A. Honecker, M.E. Zhitomirsky, R. Nath, Y. Furukawa, V.P. Antropov, Y. Singh, Phys. Rev. B 84 (2011) 094445.